Mechanical and Microstructural Analysis of Friction Surfaced Aluminum Coatings on Silicon Nitride Ceramic Substrates

H.B. ATIL, M. LEONHARDT, R.J. GRANT, and S.M. BARRANS

The lack of suitable techniques for joining Si_3N_4 ceramics with metals has limited the usage of this otherwise outstanding material for composite applications. In this study, aluminum AlMgSi0.5 (EN AW-6060) was coated onto silicon nitride Si_3N_4 ceramic substrates using friction surfacing technology. Experimental work revealed that the harmful effects of thermal shock (e.g., substrate cracking, coating delamination) observed with other material combinations can be avoided by selecting materials with a low coefficient of thermal expansion, low Young's modulus and high thermal conductivity. Design of experiments derived models for coating thickness and bonding strength fit the data well (i.e., the regression model accounts for most of the variation in the response variable). Whereas the coating thickness is predominately dependent on the rotational speed used, the bonding strength is also affected by the traverse speed. Coating thicknesses upto 2.03 mm and bonding strengths of 42.5 MPa were achieved. Deposition rates exceed those of physical vapor deposition by a magnitude of $\times 1000$ and bonding strength is on-par with thin-film metallization. Scanning transmission electron microscope analysis revealed formation of a glassy phase at the interface. Using energy-dispersive X-ray spectroscopy analysis high silicon and oxygen content with smaller percentages of aluminum and nitrogen were detected. High-resolution transmission electron microscope imaging revealed no distinct lattice structure leading to the assumption that the composition is predominantly amorphous and consists of SiAlON.

I. INTRODUCTION

THE continuous development of materials plays a very important role in industry. Increasingly, materials are used at their physical and mechanical limits and must be constantly developed to allow for increasingly demanding requirements. Two such requirements are tribological and thermal; with ceramic materials often employed when these factors are critical, gaining immense importance particularly over the last decades.[1,2] For centuries ceramic materials have been an integral part of everyday life and advances in material science have led to the development of new ceramics which, in 2018, accounted for a world-wide turnover of more than \$229 billion.[3] According to the ceramic industry, one of the biggest sectors is formed by advanced ceramics[2] which are defined as those with highly engineered and precisely specified attributes.[4] They are used in many sectors including automotive, medical and the electronics industry.[5] Components with locally differentiated material properties are becoming increasingly important, as they allow for specific adaptations that are tailored towards an application. Most of these components need to be fixed in a specific location or combined with other parts; but joining these dissimilar materials (i.e., ceramics with metals) for further use in assemblies is challenging. Due to the poor wettability of ceramics by metals it is difficult and technologically complex to join these materials. Low-cost casting processes result in poor bonding at the interface between metal and ceramic parts, and technologies currently used are complex and relatively costly. A modern solution to these problems is to use the technique of friction surfacing to apply a thick

H.B. ATIL is with the Computing and Engineering, Huddersfield University, Queensgate, Huddersfield, HD1 3DH, UK and also with Mechanical Engineering, University of Applied Sciences Kempten, Bahnhofstraße 61, Kempten, 87439, Bavaria, Germany and also with the Mechanical and Marine Engineering, Western Norway University of Applied Sciences (HVL), Inndalsveien 28, Bergen, 5063, Norway. Contact e-mails: hbah@hvl.no, hasan.atil@hud.ac.uk M. LEONHARDT is with the Mechanical Engineering, University of Applied Sciences Kempten. R.J. GRANT is with the Mechanical and Marine Engineering, Western Norway University of Applied Sciences (HVL). S.M. BARRANS is with the Computing and Engineering, Huddersfield University.

metal coating onto the surface, which in turn can be used as a base for further processing. Earlier work by the authors[6] showed that temperatures up to 580 °C can be reached during the coating process. Despite preheating the substrates, to reduce the temperature difference, micro-cracking in the substrate caused by the thermal shock was observed. The research described in this current paper investigates the use of alternative substrate materials to overcome these problems.

By way of comparison Figure 1 shows the complexity of two different metallizing techniques, (a) molybdenum-manganese metallization (Mo-Mn) and (b) thin-film metallization, along with (c) friction surfacing. The Mo–Mn method was developed nearly a century ago and is a mature process.[8] A ceramic substrate is first coated with a Mo-Mn paste, fired in wet hydrogen at 1450 °C and then plated with Nickel (Figure 1(a)). At these high temperatures a $MnAl_2O_4$ spinel is formed and the glassy phases in the Al_2O_3 substrate migrate into the pores of the metallizing layer by capillary forces, forming a strong bond by producing anchors.[9,10] By modifying this technique (e.g., paste composition, firing temperature) different ceramics can be metallized. Using a paste consisting of Ag, Pd, inorganic filler and glass Wenzel et al.[11] metallized Si_3N_4 ceramics achieving bonding strengths up to 23 MPa. Figure 1(b) shows a second commonly used metallizing process. Using physical vapor deposition (PVD) different types of metal layers can be deposited onto ceramic substrates. The metal is evaporated by heating above the gas transition temperature or sputtered by means of a process gas containing ionized particles and condensates at the surface of the substrate. Bonding mechanisms can range from mechanical interlocking to chemical bonding.[12–14] This process can also be used to apply a thin aluminum coating onto Si_3N_4 substrates as reported by Brener

et al.[15] The authors report that chemical reactions occur at the interface forming AlN layers which also increase in thickness after heat treatment.

As stated by Walker and Hodges[16] these techniques (Figures 1(a), (b)) are well developed and have been used for decades. But the need for high temperature furnaces and plating methods make them expensive; with the process itself time consuming, and not suited for high deposition rates and low quantities.

Friction surfacing of ceramics is a one step process (Figure 1(c)), provides similar strength to thin-film metallizations (e.g., PVD)[16] and does not need a furnace or atmospheric control. Friction surfacing is also suited for low quantity production and coating rates exceed those of physical vapor deposition techniques by a ×1000 magnitude. Thick-film metallization is a necessity for further connection of ceramic components to other assemblies by using common welding processes, and which is not possible by PVD. Successful application of this technique to coat Al_2O_3 ceramics with aluminum (metallizing) has been reported by Atil et al.[6] in 2020. This paper addresses the detrimental effects of thermal shock (e.g., substrate cracking) observed in the previous work and gives an overview of the selection criteria to choose the appropriate material for the process. In this study, a thick-film aluminum coating (i.e., AlMgSi0.5 / EN AW-6060) was successfully applied onto a silicon nitride Si_3N_4 ceramic substrates by using friction surfacing technology. This opens new paths for use of this material in composite applications with bonding strength and thickness exceeding what is possible with thick-film-paste metallizing technologies.[2,11]

The uneven temperature distribution in the substrate, induced by the hot coating material applied onto the surface during the coating process, leads to different
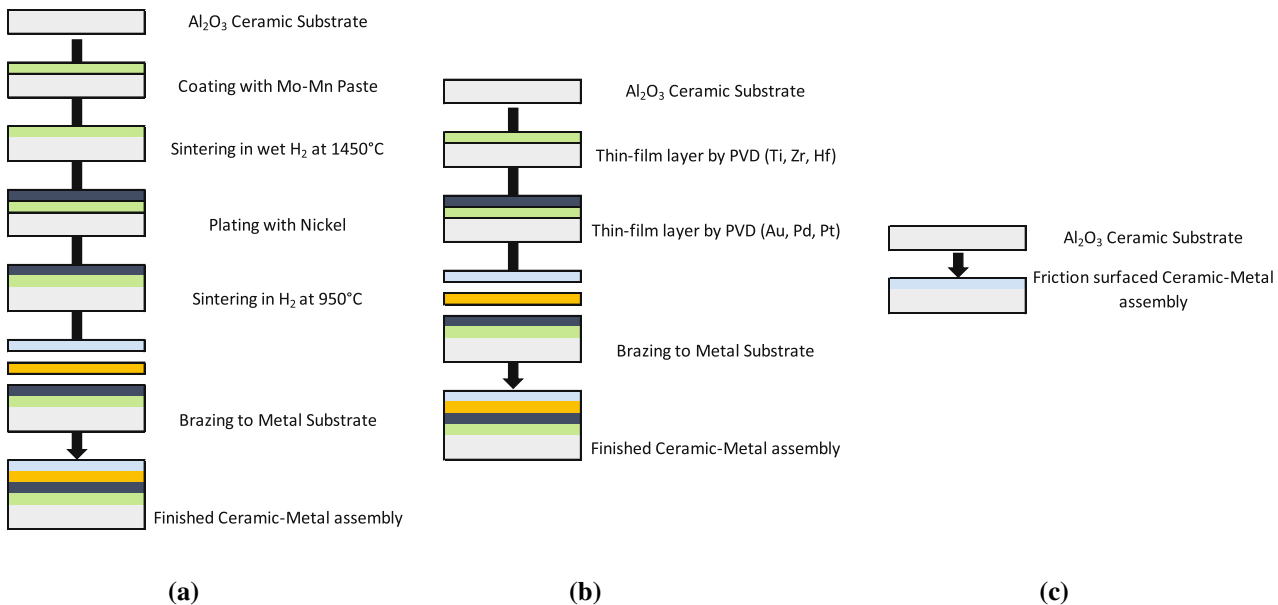

Fig. 1—(a) Molybdenum-manganese metallization,[7] (b) thin-film metallization[7] in comparison to (c) friction surfacing.

thermal expansions. This inconsistency induces stresses in the substrate material.[17] The ability of a material to withstand abrupt thermal changes is referred to as thermal shock resistance. The thermal shock resistance can be quantified by the coefficient of thermal expansion (α), the Young's modulus (E), the Poisson's ratio (v) and the prevailing temperature difference (ΔT) between the substrate and coating material during the process.

The following equation can be used to calculate the stress (σ_t)[18]:

$$\sigma_t = \frac{\alpha \cdot E}{1 - v} \cdot \Delta T \qquad [1]$$

If this value exceeds the mechanical strength (σ) of the substrate, failure occurs. Thus, for the material to remain failure free:

$$\sigma_t \leq \sigma \qquad [2]$$

Combining Eqs. [1] and [2] a value for ΔT_{max} (i.e., maximum temperature difference the material can withstand without failure) can be derived, which is equivalent to the first thermal stress resistance parameter R (also termed the thermal shock parameter of first type[19]) as suggested by Hasselman[20]:

$$\Delta T_{max} = \frac{\sigma_t \cdot (1 - v)}{\alpha \cdot E} \equiv R \qquad [3]$$

Taking the dissimilar thermal conductivities (λ) of ceramics into account, the second thermal stress resistance parameter R' (the thermal shock parameter of second type[19]) should also be considered for a direct comparison of materials[18]:

$$R' = R \cdot \lambda \qquad [4]$$

As the thermal shock resistance can be described by R and R', these material properties have been calculated for different ceramic materials and used for preselecting a suitable material combination.

Table I shows specific material properties of various ceramics and their corresponding thermal shock resistance values R and R'. Looking for the highest value for R', silicon nitride (Si_3N_4) surpasses all listed ceramics. Boron carbide (B_4C) and Silicon carbide (SiC) also present themselves as good candidates so their material properties should be considered further.

Thermal analysis previously reported[6] revealed that temperatures up to 580 °C can be reached when friction surfacing aluminum oxide with aluminum. Kılıcarslan et al.[23] found that boron carbide starts to oxidize at 500 °C whereby a protective layer of boron oxide is formed; however, this shielding effect is not enhanced at elevated temperatures[24] which leads to a deterioration of the mechanical properties. This fact and the relatively low thermal shock resistance compared to silicon nitride led to the exclusion of this, otherwise seemingly appropriate, material from further experimental analysis.

Following the same procedure for silicon carbide reveals that it is also prone to oxidation, but at higher temperatures. It forms a layer of silicon oxide which acts as a protection against further oxidation. This layer is effective up to temperatures of 1723 °C.[25] Due to the high thermal conductivity of SiC, the thermal shock parameter R' is only second to Si_3N_4; but the thermal shock parameter of first type is not on par with Si_3N_4.

Silicon nitride has the highest thermal shock resistance of all the technical ceramics displayed and it additionally sustains its strength at elevated temperatures.[26] It is used in high temperature applications such as gas turbine engines.[27] Its thermal stability at elevated temperatures, high thermal shock resistance and superior mechanical properties identifies Si_3N_4 as an excellent candidate for further research. As a result, it has been chosen as a substrate material.

The selection of a suitable coating material also strongly influences the outcome of the experiments. Not only has the coating material to be ductile and weldable, but the alloy elements should also be able to create a chemical bond with the substrate. Aluminum-magnesium-silicon alloys match the requirements, are affordable and the EN AW-6xxx group of alloys have high ductility and strength. The high silicon content improves the weldability and may increase the bonding strength by forming a chemical bond. The Magnesium content has the effect of increasing the strength by inducing age hardening[28] and additionally has the potential to increase the bonding strength by forming Mg_2Si and AlN compounds in the interface.[29] For the reasons stated above AlMgSi0.5 (EN AW-6060) has been chosen as the coating material.

Table I. Technical Ceramics with Representative Material Properties[21,22]

	Si_3N_4	SiC	B_4C	Al_2O_3	ZrO_2	TiO_2
	SN240	SC211	3MBC	A601D	Z220	T716
Flexural Strength (MPa)	1020	540	460	400	750	320
Young's Modulus (GPa)	300	430	410	380	200	270
Thermal Expansion Coefficient (10^{-6}/K)	3.30	4.40	4.50	8.00	10.50	12.10
Thermal Conductivity (W/m K)	27.00	60.00	36.00	34.00	3.00	4.00
Poisson's Ratio	0.28	0.16	0.18	0.23	0.31	0.00
R (K)	741.82	239.75	204.44	101.32	246.43	97.95
R' (W/mm)	20.03	14.38	7.36	3.44	0.74	0.39

II. EXPERIMENTAL INVESTIGATION

A. Experimental Setup and Method

For the experiments the ceramic specimens were friction surfaced using a modified milling machine (DMG Mori Co., Germany, Model: Maho MH700). This is the same set-up as used in previous work and Figure 2 shows the converted device. A high-frequency spindle drive was mounted on a carriage and, to keep the axial force constant during the surfacing process, a pneumatic cylinder was mounted between the spindle and machine head. Also, a bespoke clamping device was redesigned and manufactured (*i.e.*, adding force adjustment functionality and further enhancement on the clamping load distribution) to clamp the ceramic substrates, as shown in Figure 3. The clamping device was able to accommodate various different material sizes and shapes. Start and end-plates were milled to conform to the outer contour of the substrate, which also acted as a means of preventing specimen rotation. The clamping force can be adjusted with a screw on the clamping unit and can provide a load of up to 2.5 kN. Slots to allow for installation of heating cartridges were incorporated into the base, but were not necessary for the material combination used in these experiments.

B. Material Preparation

For these experiments, aluminum alloy rods (EN AW-6060) and ceramic plates (Si_3N_4) were cut into the required shape. The plates, as delivered, had a dimension of 50×50 mm; but due to the limited number of Si_3N_4 samples the specimens were cut into four equal rectangular parts of approximately 25×25 mm. The coating rod was initially pressed against the start-plate and then traversed over the substrate after forming a flash. This approach was used because of the small sample dimensions which dictated that a homogeneous coating should be produced across the substrate, from one side to the other. Also with this method the coating rod does not require the preparation of drilling down its rotational axis so creating a thick-walled tube, as was the case in previous work.[6] This was previously done to alleviate the local stress peaks which were induced by the rod tip at the first stage of the coating process (*i.e.*, pressing the rod onto the substrate surface) which led to surface cracks. According to Liu *et al.*[30] the generated heat at the friction zone is transferred by close contact melting towards the center of the rod forming a consistent quasi-liquid-layer between the rod and the surface of the substrate.

Figure 4 shows the dimensions of the materials used. The end surfaces of the aluminum rods were deburred and cleaned with isopropanol. The ceramic substrates were lapped to remove the sinter skin and produce a plane-parallel surface. All specimens were degreased before use.

C. Data Acquisition

Factors such as coating temperature and axial force can influence the quality of the bond[6] and these must be recorded accurately during the process. The axial force was measured with a load cell attached to the spindle, whereas the coating temperature was measured with Type K thermocouples. To get an accurate temperature reading of the coating process at the interface, the thermocouple tip had to be placed flush with the top surface of the substrate. To facilitate this, specimens were cut into two pieces incorporating a slot to hold the thermocouple.

Because of the high thermal shock resistance of Si_3N_4 substrate, unlike the previously reported work with alumina, preheating was not used. The specimens were clamped in the clamping device and the coating rod was rotated at the desired speed. Soon after pressing the rod onto the start-plate the flash started forming, whereupon the feed was started. Coating parameters were derived from earlier experiments conducted with Al_2O_3 which indicated that the coating thickness increased when high rotational speeds, high axial force and low traverse speed were used. Whereas the bonding strength improved with low rotational speed and low axial force, the traverse speed showed no significant effect. In this previous work it was observed that high axial forces led to micro-cracks beneath the surface which were detrimental to the bonding strength. Thus, the factors influencing the bonding strength should be interpreted with caution. Using these previously published coating parameters (see Atil *et al.*[6]) as a starting point, trial runs were conducted, but were unsuccessful. The coating was not consistent and no bonding to the substrate was achieved. In an attempt to improve the bonding strength
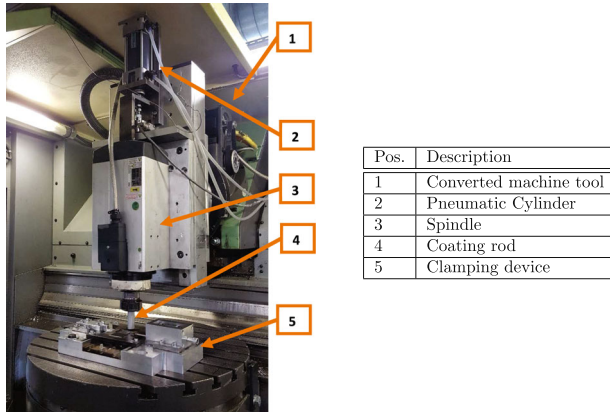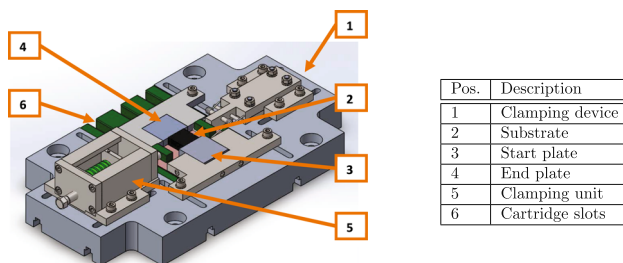

Fig. 2—Machine set-up.

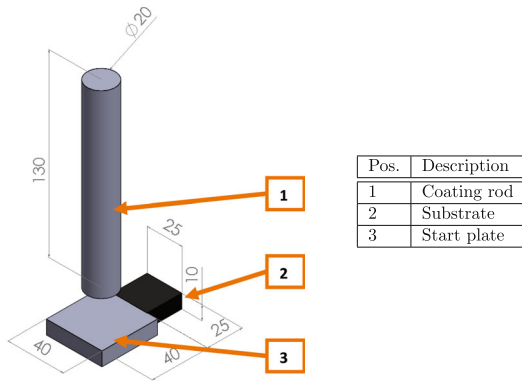| Pos.	Description
1	Converted machine tool
2	Pneumatic Cylinder
3	Spindle
4	Coating rod
5	Clamping device

Fig. 3—Clamping device.

Pos.	Description
1	Clamping device
2	Substrate
3	Start plate
4	End plate
5	Clamping unit
6	Cartridge slots

Fig. 4—Material dimensions in mm.

Pos.	Description
1	Coating rod
2	Substrate
3	Start plate

the axial force was increased which led to spindle stalls because of the greater friction between the coating rod and the substrate. Therefore, the spindle speed was increased, and successful coatings operations were then achieved. As a result of the low traverse speeds, the coating tended to be inconsistent over the complete length of the substrate. By increasing the traverse speed by 25 pct uniform deposition of the coating material was accomplished. Because of the low quantity of the specimens the varying parameters have been reduced whereby the axial force has been fixed at the maximum value (i.e., 2493 N).

D. Bonding Strength

The bonding strength was measured with an adhesion tester (DeFelsko Co., Model: Positest AT-A). The dolly had a defined stepped area on the bottom which was glued onto the coating with a high strength adhesive (HTK Ultrabond 100, HTK GmbH, Germany). Using a hollow-core drill this area was separated from the rest of the coating to make sure that only this specific area was pulled off when performing the test. Figure 5 shows one of the specimens and the detached dolly after the pull-off test.
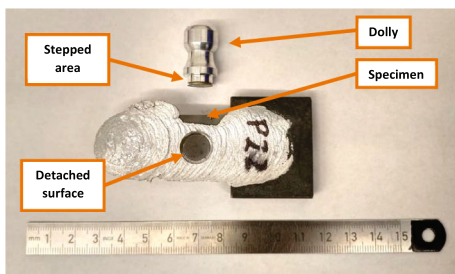
Fig. 5—Specimen with detached dolly.

E. Coating Thickness

The coating thickness was measured with a height measuring instrument (Digimar-817, Mahr GmbH, Germany) on four points with a probe (Figure 6(a)) and the mean value found. Figure 6(b) shows the specimen and the corresponding measurement points.

F. Design of Experiments (DoE)

As with previous work, Design of Experiments (DoE) tools were used to investigate the effects of the coating parameters on the coating thickness and bonding strength. To minimize the quantity of specimens needed the process parameters have been reduced to two, and a two-level full factorial design was chosen. To identify if curvature in the response is present center points were added. By using only two input factors, one center point and four replications, the total number of successful specimen tests required was calculated to involve 22 samples. These can be summarized as four parameter sets with four replicates and one additional parameter set used for the center points with six replicates.

Table II shows the parameters used for the new experiments.

The objective of the experiments conducted was to identify the effects of the process parameters, rotational speed and traverse speed, on the response, bonding strength and coating thickness. These process parameters are related to physical variables such as temperature and pressure which in turn influence the achievable bonding types. The DoE analysis is, in this case, a means-to-an-end to investigate the relationship between process parameters, physical variables and binding mechanisms. The results of the experiments were fitted into a regression model which can also be used for predicting new sample data.

G. Thermal Shock

Despite the high-thermal shock resistance of the Si_3N_4 substrate material (i.e., $R = 768$ K[31]) additional thermal shock tests were conducted. For this purpose special test equipment was used where Figure 7(a) shows the apparatus and Figure 7(b) the specimens placed on the sample holder. The test geometry was chosen so that the thermal shock tests reflected the loading case during the coating experiments and measured $\varnothing$ 25 mm $\times$ 10 mm. These were cut from a 25 mm diameter rod, lapped to remove the sinter skin and irregularities caused by the cutting process; the perimeter was chamfered to eliminate the effect of stress concentrations due to defects introduced during material preparation.

The samples were heated up to the various required thermal shock temperatures (i.e., representative friction surfacing temperature of 600 K discussed in Section III–C, thermal shock parameter of first type 770 K, and maximum temperature 1000 K) with a heating rate of 10 °C/min in the tube furnace. To achieve a uniform temperature through the material bulk, the specimens were held in the furnace for a period of 10 minutes after reaching the desired temperature where
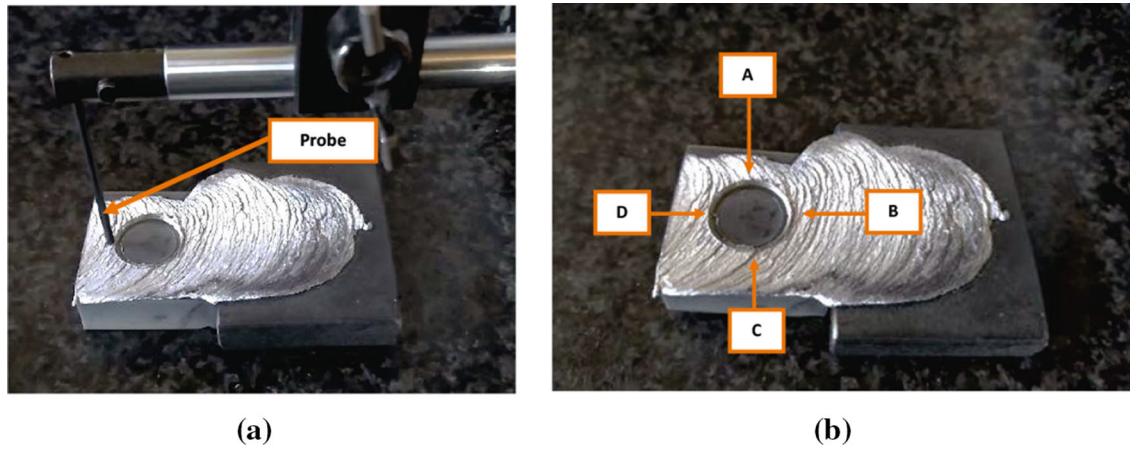
Fig. 6—Measuring instrument showing (a) probe and (b) coating thickness measurement points.

Table II. Coating Parameters

	Levels		
Factors	Low	Center	High
Rotational Speed (rpm)	4000	5000	6000
Traverse Speed (mm/min)	200	300	400

Fig. 7—Thermal shock tests: (a) apparatus and (b) sample holder with Si$_3$N$_4$ samples in place.

upon they were quenched in the quench medium (i.e., water at 22 °C). After a period of 3 minutes the specimens were removed from the bath and dried in a laboratory oven at 120 °C for 2 hours and set aside for cooling down at ambient air conditions (22 °C). A dye penetration test (MR-313DL, MR Chemie GmbH, Germany) was carried out to improve the visibility of the cracks. Figure 8 shows a tested specimen with applied dye penetration test.

The specimens were cleaned with a universal cleaner (MR-79) then penetrant was applied onto the surface (MR-313DL) with any excess removed using water. A developer (MR-70) was applied onto the surface to improve the visibility of any cracks that had been formed. The penetrant will indicate a wider and deeper crack by showing a wider and more intensive dye color on the surface of the specimen.[32] As the developer conceals the crack path it was removed to permit further analysis of the specimens.

III. RESULTS AND DISCUSSION

A. Coating Thickness

In the samples prepared as previously described, the coating thicknesses were seen to vary from 0.76 to 2.03 mm; depending on the process parameters used. To simplify the presentation in the tables and equations, abbreviations for rotational speed (r) and traverse speed (f) have been used.

Using the response data of the experiments a simple multiple linear regression model (i.e., least squares fit) was developed. The calculated model for the coating thickness is as follows:

$$\text{Coating thickness} = 2.32 - 2.39 \times 10^{-4} \cdot r \quad [5]$$

Looking at Figure 9 the results at the five parameter sets used are shown as dots along with the calculated linear regression surface derived from the model. Examining the plot, five datapoints (P1, P3, P9, P14 and P18) can be identified which have relatively high residuals (i.e., high deviation from the model prediction). Checking the parameter set repetitions, response and surface structure of the coating, datapoint P9 was identified as an outlier. A visual examination of the specimen evidenced a
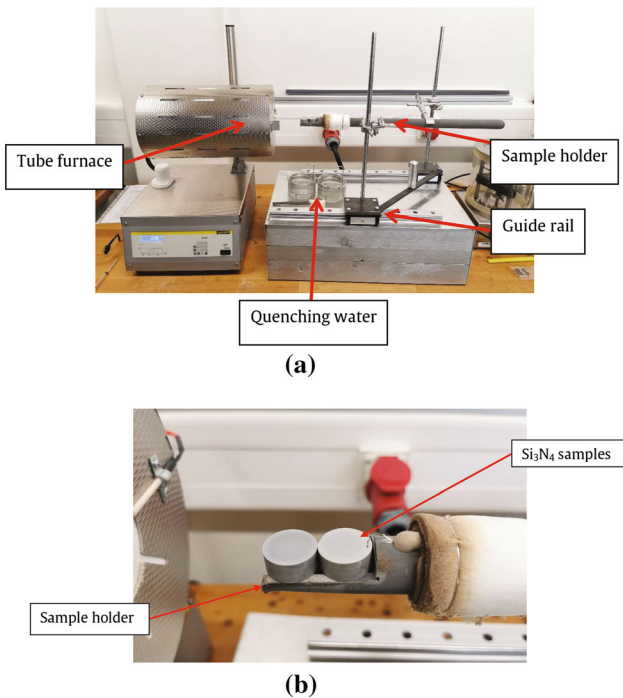
Fig. 8—Specimen with applied dye penetration test.

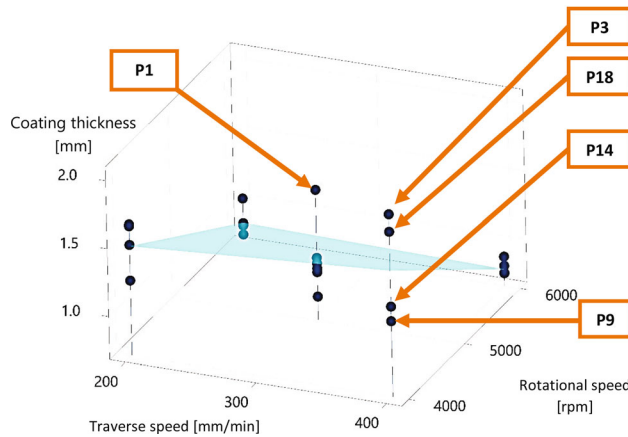
Fig. 9—3D-scatterplot and linear regression surface of coating thickness *vs* traverse speed *vs* rotational speed.

Table III. Analysis of Variance: Coating Thickness

Source of Variance		P Value
r (Rotational Speed)		<0.001
f (Traverse Speed)		0.723
r*f		0.496
Curvature		0.608
Lack-of-Fit		0.948
Model Summary	S	R-sq
	0.234673	71.66 pct
Model Summary	S	R-sq
	0.173812	84.65 pct

smeared (coating) surface structure which could have been a result of spindle speed fluctuations at lower rotational speeds. This was not observed on any of the repetitions for this parameter set and thus was removed from the analysis, whereas datapoint P1 had a large residual non-representative measurement attributed to a burr on the coating. No reasons for dismissing datapoints P3, P14 or P18 were found: the surface structure and coating measurement showed no evidence of error. But the fact that all the points with a traverse speed of 400 mm/min and rotational speed of 4000 rpm shows a high deviation from the model prediction, indicates that using this parameter set the process becomes unstable.

To quantify the significance of the parametric change on the coating thickness an analysis of the variance was made which is shown in Table III. P values higher than the confidence level ($\alpha = 0.05$) are assumed to not have a significant effect on the response.[33]

As can be seen, only the rotational speed has a significant effect on the coating thickness showing a P value < 0.001, whereas the traverse speed and the two-way interaction of both parameters does not have a significant effect. Looking at the lack-of-fit P value, which is relatively high at 0.948, indicates that the

regression model fits the underlying data.[34] Also no curvature was detected (*i.e.*, P value < 0.05).

Checking the model summary, R-sq (a measure for the accuracy of the regression model) is relatively high with 71.66 pct; but lower than what was achieved in previous work using an aluminum oxide substrate[6] (81.32 pct). By removing datapoint P9 and correcting datapoint P1 (*i.e.*, remeasuring) the R squared value increased by 13 pct to R-sq = 84.65 pct. Using the corrected response data of the experiments including center points (CtPt), the calculated model (*i.e.*, linear least squares fit) for the coating thickness is as follows:

$$\text{Coating thickness} = 1.867 - 1.61 \times 10^{-4} \cdot r \quad [6]$$

From Eq. [6] the response can be calculated by inserting the values for the rotational speed r and the traverse speed f. The center point variable CtPt is either 1, if the center values for r and f are used (see Table II), or 0 otherwise; shifting the regression model to fit the data at this midpoint.

By constructing a Normal Probability Plot the distribution of the data were assessed to be normal.

To get a better view of the interactions between the parameters an interaction plot for the coating thickness was constructed (see Figure 10). Evaluating the plot, it can be seen that at higher rotational speeds the coating thickness decreases, and the influence of the traverse speed is not significant. While at lower rotational speeds the process becomes unstable and, because of the wide error band, the influence of the traverse speed to the coating thickness can not be determined reliably.

This is in marked contrast with what was reported for aluminum oxide-aluminum specimens where it was discovered that at higher rotational speeds and low traverse speeds coating thickness was the greatest.[6] This was explained by the increase of frictional area at the inner diameter of the rod due to the removal of the core material so forming a thick-walled tube. By doing so, an extra space was created at the center of the rod for the flash to flow and form, which in turn increases the frictional area. The current experimental results would seem to validate this reasoning, as by not removing the inner diameter of the coating rod no additional area for contact and disposal of material is present. Thus, increasing the rotational speed only increases the flash
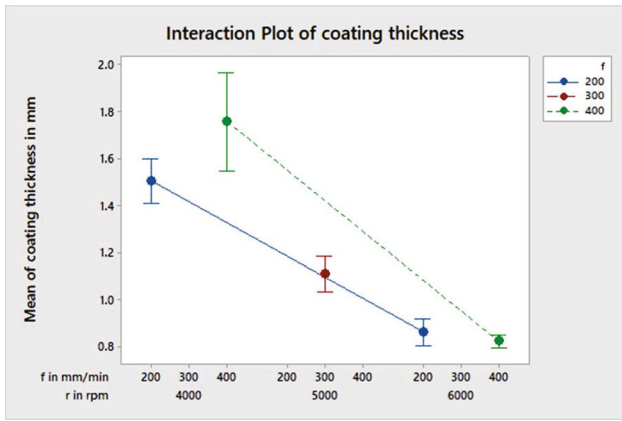
Fig. 10—Interaction plot of coating thickness as a function of rotational speed (r) and traverse speed (f).
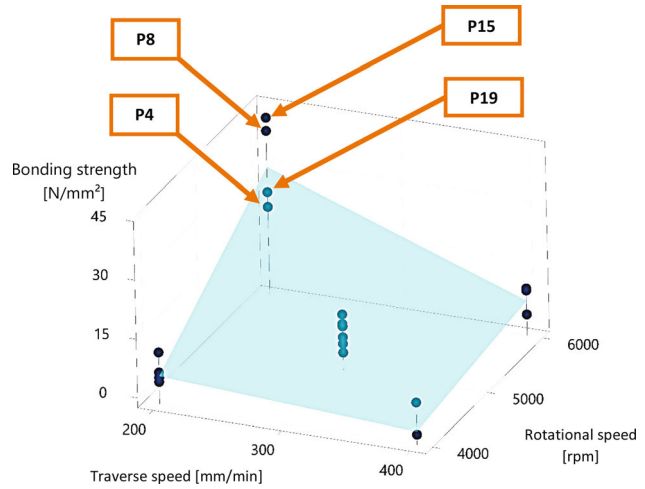

Fig. 11—3D-scatterplot and linear regression surface of bonding strength *vs* traverse speed *vs* rotational speed.

material. This is also in line with what has been published concerning friction surfacing of metals.[35,36]

B. Bonding Strength

Tests of bonding strengths made on the specimens were found to vary from 1.8 up to 42.5 MPa. The calculated simple regression model (*i.e.*, linear least squares fit) for the bonding strength is as follows:

$$\text{Bonding strength} = -82.7 + 2.27 \times 10^{-2} \cdot r + 18.1 \times 10^{-2} \cdot f - 5.00 \times 10^{-5} \cdot r \cdot f \quad [7]$$

Figure 11 shows the 3D-scatterplot and linear regression surface of the results.

Unusual observations can be seen at datapoint P4, P8, P15 and P19 (*i.e.*, high deviation from the model prediction). Examination of the coated specimens and their corresponding dollies provides no satisfactory evidence for dismissing these points.

Table IV shows the corresponding *P* values and the model summary.

It can be seen that both test parameters of rotational speed and traverse speed, as well as their two-way interaction, are significant (*P* value < 0.05). Again, no curvature was detected (*i.e.*, *P* value < 0.05) and lack-of-fit is not significant. Compared with earlier findings from aluminum oxide-aluminum specimens which showed an *R*-sq value of only 24.52 pct,[6] this model summary has a relatively high *R*-sq value of 80.20 pct; so the regression model accuracy increased significantly.

The calculated regression model for the bonding strength, including center points, is as follows:

$$\text{Bonding strength} = -81.3 + 2.27 \times 10^{-2} \cdot r + 18.1 \times 10^{-2} \cdot f - 5.00 \times 10^{-5} \cdot r \cdot f - 4.88 \cdot CtPt \quad [8]$$

Table IV. Analysis of Variance: Bonding Strength

Source of Variance		*P* Value
r		<0.001
f		<0.001
r*f		<0.001
Curvature		0.101
Lack-of-Fit		0.839
Model Summary	*S*	*R*-sq
	5.86353	80.20 pct

It was previously noted that cracking of the substrates due to high coating temperatures and low thermal shock resistance led to poor data correlation and a low R-sq value. By using Si_3N_4 as substrate material, which has the highest thermal shock resistance of all technical ceramics, the lack of post-test surface cracks would seem to confirm this assumption. The acquired data would not have been influenced by an unaccounted factor, namely cracking, and so showed a greater consistency. Essentially, what was being tested in the pull-off tests was previously not always a separation of the coating from the substrate; but between layers of the substrate due to micro-cracks beneath the surface.

Data distribution was classed as normal and checked by utilizing a Normal Probability Plot. As stated above all factors and their two-way interactions have a significant effect on the response. To get a better view of these interactions an interaction plot (see Figure 12) was constructed. It can be seen that traverse speed has a slightly greater impact on the bonding strength than the rotational speed; but they are otherwise quite similar.

Looking at the plot it is clear that increasing the rotational speed will increase the bonding strength, whereas increasing the traverse speed will decrease the bonding strength. Highest values for the response can be achieved by increasing the rotational speed and decreasing the traverse speed. This is most likely caused by the
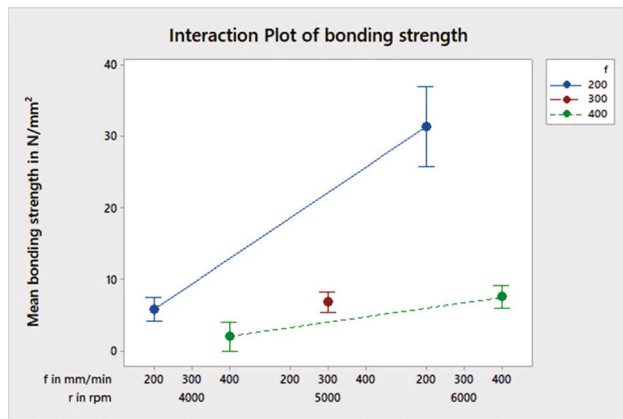
Fig. 12—Interaction plot of bonding strength.

heat generated during the process. By increasing the rotational speed, and similarly by decreasing the traverse speed, more heat is generated in the friction zone: this surplus heat can be transferred to the interface increasing the bonding strength. This is in line with publications in the area of friction welding of ceramics where higher rotational speeds tend to increase the bonding strength.[37,38]

In conclusion to the DoE analysis, it can be said that using a ceramic substrate material with a high thermal shock resistance is beneficial for the process. High bonding strength and coating thicknesses can be achieved without damaging the substrate.

C. Thermal Analysis

This section considers an evaluation of the thermal conditions prevalent during friction surfacing which is not directly controlled by the input parameters r and f, but is a peculiarity of the process itself. According to Liu et al.,[30] who applied contact melting theory to friction surfacing, the temperature at the interface reaches a stable plateau during friction surfacing which is close to the melting point of the coating rod because an equilibrium is established between melting and solidification of the material. According to Edelman et al.[39] and Brener et al.,[15] who studied interfacial reactions of Al/Si_3N_4 systems, AlN-like layers can occur and increase in thickness when increasing the temperature up to 600 °C. So, in order to evaluate likely chemical reactions it is necessary to establish the magnitude of the peak interface temperatures during the surfacing process. In our case this may affect bonding strengths and has been analyzed in this section. Again, it follows the methodology previously used and detailed in a past article.[6]

Figure 13 shows two examples of the temperature readings for the tests made at 6000 rpm, and a traverse speed of 200 mm/min and 400 mm/min (0-distance traveled is the datum at the center of the starting plate).

It can be seen that the lower traverse speed (blue plot, left hand side) shows a higher maximum temperature, but the readings are in a similar range when compared

with the higher traverse speed (i.e., 567.08 °C and 584.37 °C) with a temperature difference of only 17.29 °C.

By repeating the temperature tests at the specified parameters, minimum/maximum values and the corresponding mean were determined. The mean value for three specimens tested at 6000 rpm and 200 mm/min was calculated to be 585.60 °C with a standard deviation of ±3.60 K whereas three specimens tested at 6000 rpm and 400 mm/min was calculated to be 563.56 °C with a standard deviation of ±12.97 K. The results from specimens tested at 6000 rpm and a traverse speed of 400 mm/min demonstrate a larger spread which was assessed as being due to movement of the thermocouples. In addition, higher traverse speeds reduce the thickness of the quasi-liquid layer between the rod and the substrate which could lead to increased friction when a greater portion of this layer is deposited on the surface, with shearing forces affecting the thermocouple readings. On the other hand, lower traverse speeds lead to an increase in heat generated at the friction zone and an increase in the thickness of the quasi-liquid layer which, in turn, increases the temperature readings. Looking at the ternary phase diagram of the coating material (AlMgSi0.5) there is no significant change in the percentage of the liquid phase at the logged min/max temperatures. As stated by Liu et al.[30] this is due to the fact that the friction zone is not located at the substrate surface, where the temperature was measured, but above the deposited coating. The quasi-liquid layer is formed between the friction zone and the deposited material, and consists of liquid and solid material alike. Thus, lowering the traverse speed may increase the temperature at this layer increasing the thickness of the quasi-liquid layer.

D. Thermal Shock Analysis

Using Si_3N_4 with a thermal shock resistance parameter of first type R of 768 K no cracks have been found in the substrate and the pull-off dollys showed no evidence of surface breakouts remaining on the deducted areas.

To get a more accurate overview of the thermal shock behavior, further thermal shock tests with ΔT of 600 K, 770 K and 1000 K were conducted. Due to the rapid change in temperature during the coating process, differential expansion and contraction can induce stresses in to the substrate leading to a weakening of the grain boundaries and crack growth, negatively affecting the strength.[40]

Figure 14 shows the tested specimens. To increase the visibility of the cracks a dye penetrant test, as described in Section II–G, was carried out.

Shifting focus to the findings in Section III–C, temperatures upto 585.60 °C ± 3.60 K were measured during the coating process. These temperatures seem to have no detrimental effect on the material. This behavior is confirmed by the thermal shock tests carried out at $\Delta T = 600$ K (Figure 14(a)) which show no evidence of crack formation. Increasing the temperature up to the
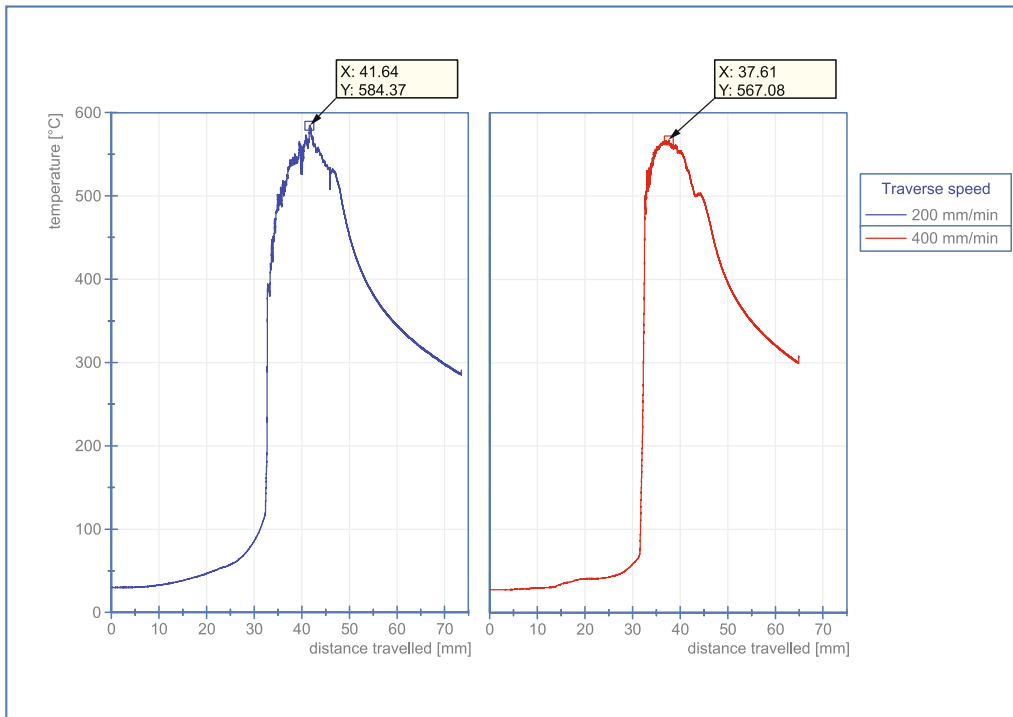
Fig. 13—Thermal plot for rotational speed of 6000 rpm and traverse speed of 200 mm/min and traverse speed of 400 mm/min.
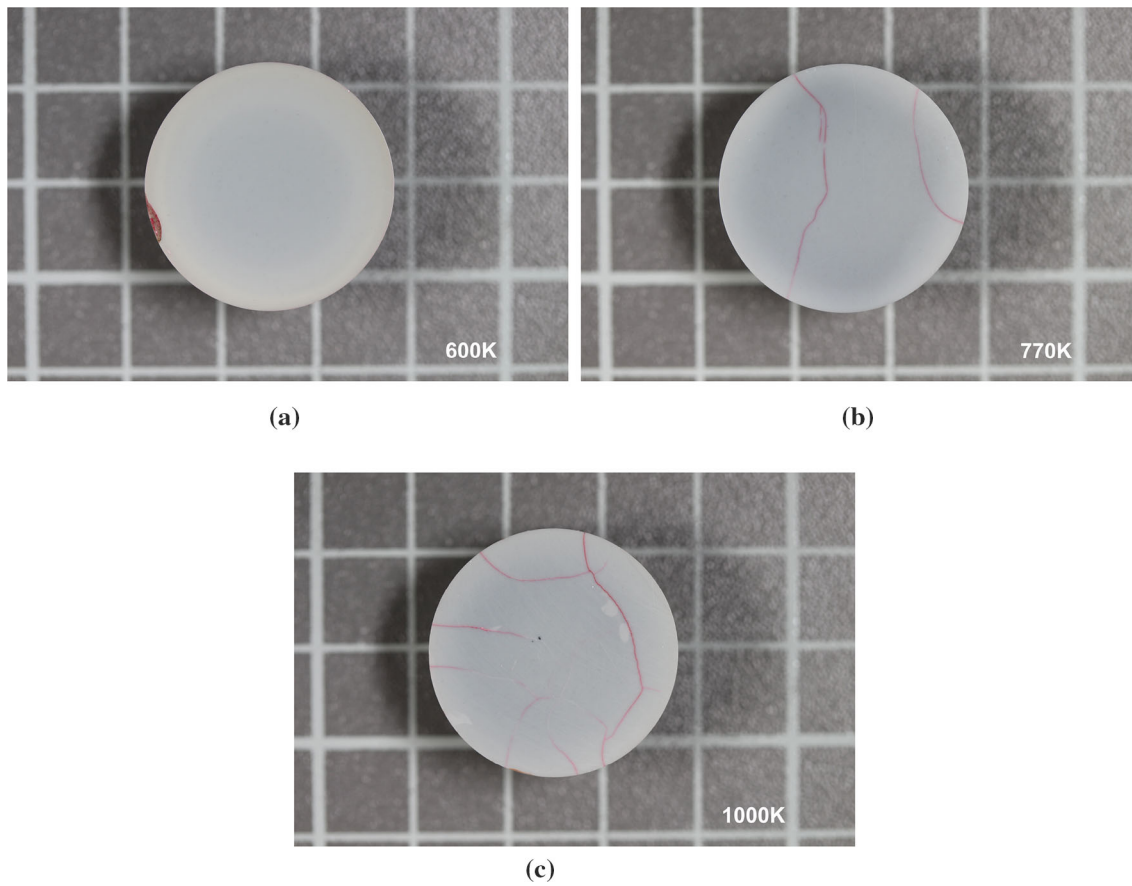

(a)

(b)

(c)

Fig. 14—Thermal shock tested specimens at (*a*) 600 K, (*b*) 770 K and (*c*) 1000 K temperature difference with applied penetrant.

thermal shock parameter of first type $R = 768$ K (Figure 14(b) with $\Delta T = 770$ K) cracks started to form. Further tests revealed that an extreme temperature change with $\Delta T = 1000$ K, exceeding the thermal shock parameter of first type by 330 K, will drastically increase the number of initiated cracks, see Figure 14(c). Although the material used has a thermal shock resistance of 768 K, cracks were observed in the tested specimens for this temperature range. This is related to the defect distribution within a volume and the failure probability of ceramics which will be discussed in more detail.

According to Carter et al.[2] mechanical properties of ceramics are dependent on the defect size and distribution and can vary within a material: this is described by the Weibull distribution.[41] By transferring the Weibull distribution to material strength, the failure probability (P_f) can be calculated as follows[42]:

$$P_f(\sigma) = 1 - \exp\left[-\left(\frac{\sigma}{\sigma_0}\right)^m\right] \quad [9]$$

where σ is the measured flexural strength, m the Weibull modulus and σ_0 the characteristic strength for a failure probability of 63.2 pct. These values are determined by the manufacturer during production and are most often listed in the datasheet accompanying the material. Using these values a failure probability can be calculated for a desired flexural strength or vice versa. Due to the fact that the defect distribution and thus the mechanical strength in ceramics is dependent on the volume of the tested specimens, part geometry is regulated by standards such as ASTM C 1161-18,[43] ASTM C 1499-19,[44] and DIN EN 843-1.[45] Upon consultation with the manufacturer (3M Deutschland GmbH, Germany), the Weibull modulus ($m = 13.3$) and the characteristic strength for the used Si_3N_4 ceramic material ($\sigma_0 = 827 MPa$) was provided. These values were determined by the manufacturer using rectangular beam specimens and a four-point bending apparatus. Due to the different specimen geometry used for the thermal shock tests, these values could not be used directly. According to Lube et al. and Danzer et al.[46,47] uniaxial and biaxial strength tests for Si_3N_4 specimens follow the same volume dependency. The characteristic strength of the beams can be used to predict the characteristic strength of the cylindrical specimens. Two effects need to be considered for a comparison. Because of the different stress states for an uniaxial and biaxial load, in the first step, an equivalent stress ($\sigma_{0,eq}$) needs to be calculated for the reference characteristic strength ($\sigma_{0,beam}$). This is done using the principle of independent action[48] and is given by the following equation:

$$\sigma_{0,eq} = (\sigma_I{}^m + \sigma_{II}{}^m + \sigma_{III}{}^m)^{1/m} \quad [10]$$

where σ_I, σ_{II} and σ_{III} are the principal stress components. For an uniaxial stress state only one principle stress component is involved thus:

$$\sigma_{0,eq} = (\sigma_I{}^m)^{1/m} = \sigma_0 \quad [11]$$

For cylindrical ball on three balls test specimens, Danzer et al.[47] observed that a biaxial stress state is generated and used Eq. [10] to determine the equivalent characteristic strength. They demonstrated that, accounting for volumetric effects (see below), the characteristic strengths from ball on three balls tests were directly comparable to those determined from bending tests. According to Staudacher et al.[49] results obtained from different biaxial strength measurements (i.e., ring on ring test and ball on three balls test) deliver comparable results. For the thermal shock test considered in this work, sudden chilling of the cylindrical test piece will generate a similar biaxial stress state on the surface. Thus, in the second step, the influence of the volumetric effect needs to be considered. To transfer the strength values to another part geometry (i.e., volume), the following equation was used[50]:

$$\frac{\sigma_0}{\sigma} = \left[\frac{V_{\mathrm{eff}}}{V_{0\,\mathrm{eff}}}\right]^{1/m} \quad [12]$$

where $V_{0\,\mathrm{eff}}$ is the effective volume of the tested specimen with the corresponding characteristic strength σ_0, V_{eff} the effective volume of the part to which the strength value is transferred to and σ the transferred characteristic strength. The strength in both cases is related to the effective volume and thus can be used to extrapolate the characteristic strength for a different volume.

The effective volumes can be calculated as follows[51]: For the four-point bending test:

$$V_{0\,\mathrm{eff}} = \left[\left(\frac{L_i}{L_o}\right)m + 1\right] \cdot \left[\frac{1}{2(m+1)^2}\right] \cdot [b \cdot d \cdot L_0] \quad [13]$$

where L_i is the inner load span, L_o is the outer load span, b is the section breadth of the beam and d the section depth.

For the cylindrical specimens used in this work:

$$V_{\mathrm{eff}} = \frac{\pi}{2} \cdot D_L{}^2 \left\{ 1 + \left[\frac{44(1+v)}{3(1+m)}\right] \cdot \left[\frac{5+m}{2+m}\right] \cdot \left(\frac{D_S - D_L}{D_S D}\right)^2 \right.$$
$$\left. \cdot \left[\frac{2D^2(1+v) + (D_S - D_L)^2(1-v)}{(3+v)(1+3v)}\right] \right\} \cdot \left[\frac{h}{2(m+1)}\right] \quad [14]$$

where D_L is the diameter of the loading ring, D_S the diameter of the supporting ring, D the disc diameter and h the disc height.

Table V. Calculated Failure Probability P_f for Conducted Thermal Shock Test

ΔT (K)	σ_t (MPa)	P_f (Pct)
600	625.00	≈ 4.33
770	802.08	≈ 70.57
1000	1041.67	≈ 100.00

Using Eqs. [12], [13], [14] and part geometry data (i.e., $L_i = 20$ mm, $L_o = 40$ mm, $b = 4$ mm, $d = 3$ mm, $D_L = 5$ mm, $D_S = 11$ mm, $D = 25$ mm, $h = 10$ mm) the characteristic strength for the tested specimens was calculated. This value can be used to estimate the failure probability of the thermal shock specimens using Eqs. [1] and [9[. The results are listed in Table V.

The calculated values reflect the results from the thermal shock tests. For a thermal shock of $\Delta T = 600$ K a failure probability of 4.33 pct was estimated. As already mentioned examining the specimens for this temperature no cracks were found. Whereas the specimens with an induced thermal shock of $\Delta T = 770$ K showed first signs of crack formation. None of these specimens remained undamaged. This is attributed to the high failure probability of $P_f \approx 70.57$ pct at this temperature and explains why a thermal shock of 770 K causes crack initiation. For the specimens quenched at $\Delta T = 1000$ K a drastic increase in crack formation was observed. This is also in line with the estimated failure probability of $P_f \approx 100.00$ pct. The material is not capable of withstanding these stresses. Examination of the specimens revealed that the form of the cracks exhibit signs of radial propagation, starting from the specimen surface and stretching towards the center of the samples with additional fractures running through the material. This is due to the rapid cooling that first takes place on the specimen surface of the material making contact with the quenching medium. While the core of the material still retains a high temperature, the outer surface cools down abruptly. This induces tensile stress at the specimen surface and compression stress at the center where a combination of the local stress state and material structures provide a crack initiation site. Because of the mixed fracture type, volume defects as well as surface defects are most likely the cause for failure of the tested specimens at 770 K. Whereas additional crack initiation through grain boundary weakening is most likely the reason for failure at 1000 K.
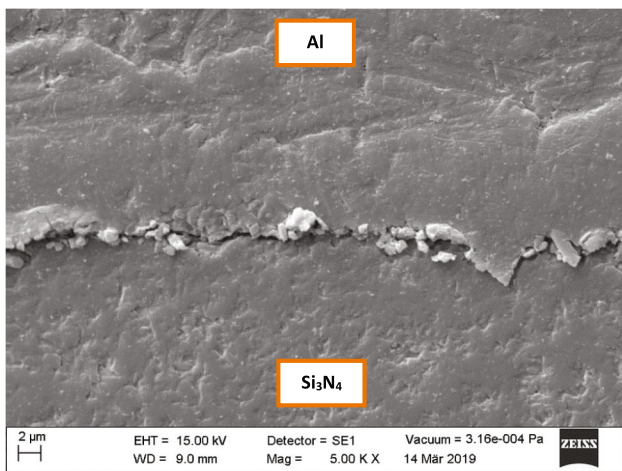
Fig. 15—SEM image of Si_3N_4–Al interface.

It should be noted that the thermal shock temperature indicated in the datasheet can be misleading. This is most often calculated for the mean tensile strength and is characterized by a very high failure probability which should be taken into account for high temperature applications of the selected material.

E. Microscopy and EDX Analysis

Figure 15 shows a SEM image of the interface for the aluminum alloy coated Si_3N_4 substrate using 6000 rpm and 200 mm/min as coating parameters. Using secondary electron contrast on the SEM the surface structure at the interface can be seen. Preparation of the specimen proved to be difficult because the ductile aluminum showed tendency to smear onto the hard surface of the silicon nitride substrate during the polishing process. This also led to a step formation at the interface which can be identified by the brighter contrast in the image. Changing the detector type on the SEM from secondary electron to backscatter, showing material contrast, reveals a clear separation of the interface without evidence of a diffusion zone (Figure 16(a)).

Figure 16(b) shows an energy dispersive X-ray spectroscopy (EDX) analysis of the substrate-coating interface. As can be seen at the interface nitrogen is missing at Point 3, with the aluminum content dropping to 16 pct and silicon content increasing to 84 pct. This could be an indication for a chemical reaction and forming of new compounds; however, this could not be verified by further SEM examinations as nitrogen, which is an element of low atomic mass, is extremely difficult to detect by SEM and EDX-Analysis.[52] Measuring the elements at different positions revealed that only 2 out of 10 measurements reproduced this result.

To overcome the difficulties described above (e.g., material preparation, interface image resolution, nitrogen detection) further analysis of the interface and bonding mechanisms has been conducted by scanning transmission electron microscopy (STEM) and EDX. Looking at Figure 17 it can be seen that the aluminum coating forms a bond with the Si_3N_4 substrate at several positions (1-4). These spots have been analyzed in more detail.

Comparing the bright field (BF) images of the individual spots in Figures 18(a) through (d) one major peculiarity is apparent in all areas; a glassy phase connecting the interface. Whereas spots 1 to 3 are still connected, spot 4 shows a hook-like structure which has been separated. This could be due to the different thermal expansion coefficients of the constituent materials and the resulting stresses induced during the cooling phase after the coating process.

EDX analysis of the spot 1 and spot 4 glassy phase reveals a high silicon and oxygen content with a smaller percentage of aluminum and nitrogen as shown in Figures 19(a) and (b). respectively. It should be noted that C, Pt and Ga signals are due to sample preparation and the Cu signal originates from the Cu TEM-Grid used. To identify the composition of the interface region further analysis is needed; therefore HRTEM imaging
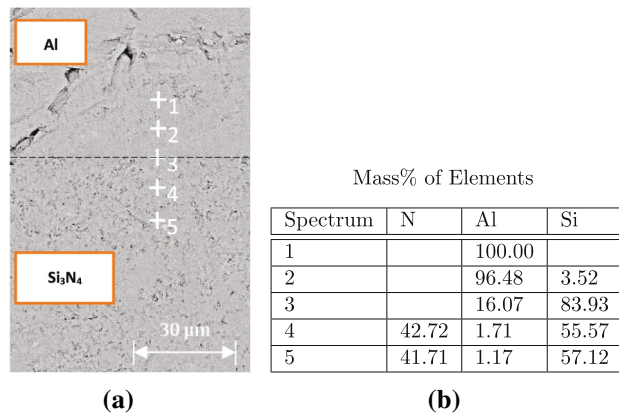
Fig. 16—Backscatter image of (*a*) Si_3N_4–Al interface and (*b*) EDX analysis.

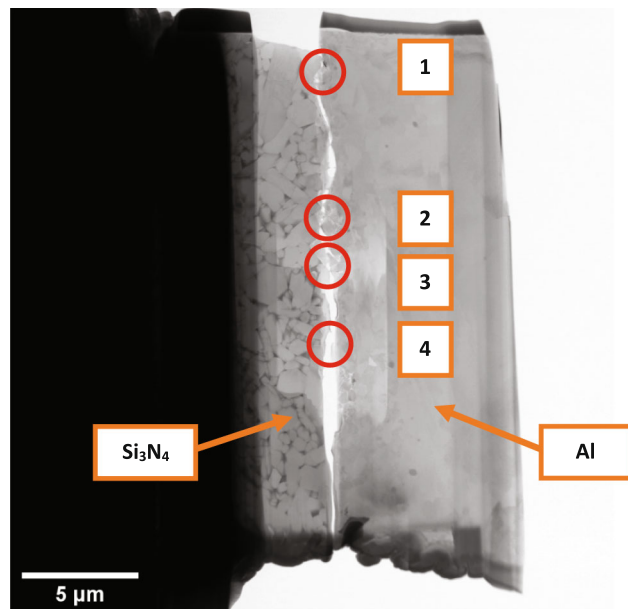| Spectrum	N	Al	Si
1		100.00	
2		96.48	3.52
3		16.07	83.93
4	42.72	1.71	55.57
5	41.71	1.17	57.12

Mass% of Elements

Fig. 17—TEM image of Si_3N_4–Al substrate.

has been used. No distinct lattice structure could be perceived. The composition is predominately amorphous and the EDX is showing remains of both materials (*i.e.*, coating and substrate). This leads to the assumption that amorphous SiAlON forms during the process at the interface, bonding the coating to the substrate. To ensure that the compounds were not already present on the surface before the coating process, additional samples (*i.e.*, before and after coating process) were analyzed.

Figure 20(a) shows a SEM image of the Si_3N_4 substrate before the coating process and Figure 20(d) after the coating process with the coating removed. Quantitative results of the EDX analysis can be seen in Figures 20(d) and (e) , whereas the EDX spectra are shown in Figures 20(c) and (f) respectively. It should be noted that C and Au signals are due to sample preparation. For easy comparison bar plots have been

used for the quantitative mass percent results. Comparing the green bars which represent the oxygen mass percentage and the blue bars which represent nitrogen mass percentage it can be seen that the surface oxides and nitrides increase significantly after the coating process. This can also be seen in the EDX spectra (Figures 20(c) and (f)). The element peak intensity of oxygen and nitrogen increases after the coating process. According to Potts *et al.*,[53] these peaks are approximately proportional to the mass percent of the elements measured. This confirms the assumption that the compounds were not already present on the substrate surface before the coating process and that amorphous SiAlON forms during the coating process at the interface.

Further analysis of the specimens was conducted by removing the coating from the substrate and analyzing the substrate surface. Figures 21(a) through (e) show these specimens and their corresponding coating parameters (*i.e.*, 4000–6000 rpm and 200–400 mm/min).

Upon examination of the specimens that had their coatings pulled-off, dark areas were identified on the substrate surfaces; of which an increase in size and quantity was observed with increasing rotational speed. Whereas an increase in traverse speed showed the opposite effect, namely a reduction in size and quantity. EDX analysis of the dark areas, in comparison to the bulk material, showed no change in composition. Despite decreasing the acceleration voltage of the SEM, thus reducing the interaction volume, a change in element mass percentage was not detectable. This was attributed to the thickness of the remaining dark layer. In contrast, a different result emerged from the analysis of the pull-off dollys. Figure 22(a) shows the SEM image of a pull-off dolly with the spot locations for the EDX analysis.

Checking the quantitative results of the EDX analysis in Figure 22(b) at spot 4 and spot 3 the aluminum alloy used for manufacturing the dollys can be identified. Whereas spot 2 and spot 1 show a high silicon, aluminum, oxygen and nitrogen content which can also be seen in the EDX spectrum graph for spot 1 (see Figure 22(c)). Looking at spot 4 and spot 1 with a higher magnification a change in the surface structure is revealed (Figures 23(a) and (b)).

This is in line with the TEM and EDX results (see Figures 19(a) and (b)), again confirming that SiAlON forms during the coating process at the interface. Examining the surface structure and corresponding dollys of the coated specimens no interface reaction was observed for low rotational speeds and high traverse speeds. Whereas by increasing the rotational speed and lowering the traverse speed an increase in bonded area was observed (see Figures 21(a) through (e)). As already mentioned in Section III–B this is most likely caused by the heat generated during the process. By increasing the rotational speed and decreasing the traverse speed, more heat is generated in the friction zone: this surplus heat is transferred to the interface supporting chemical reaction and thus increasing the bonded area.

According to Brener *et al.*[15] who studied interfacial reactions in Al/Si_3N_4 thin-film systems, Al can reduce
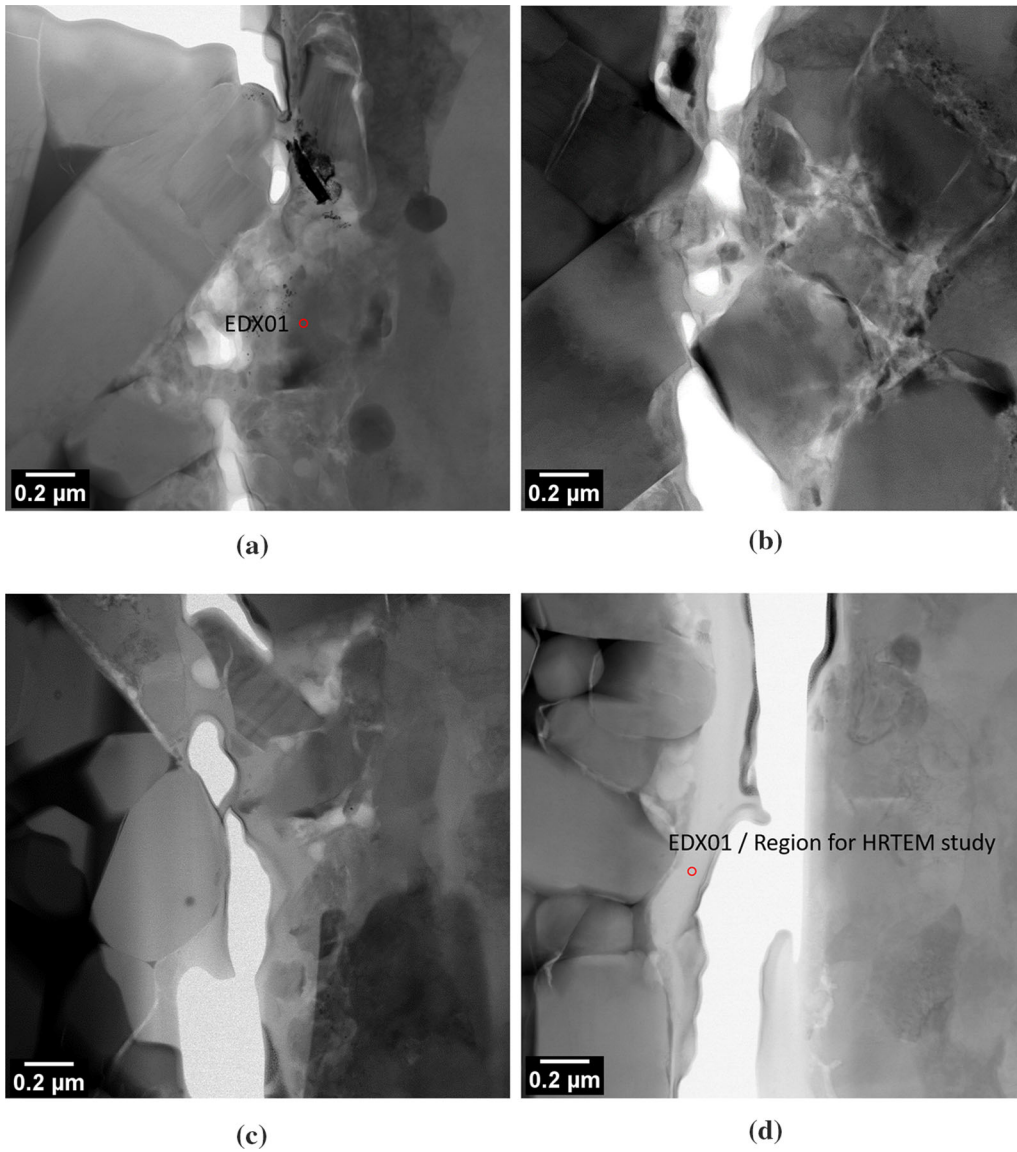
Fig. 18—STEM bright field (BF) image of (*a*) spot 1 with marked EDX area (*b*) spot 2 (*c*) spot 3 and (*d*) spot 4 with marked EDX area and HRTEM study region.
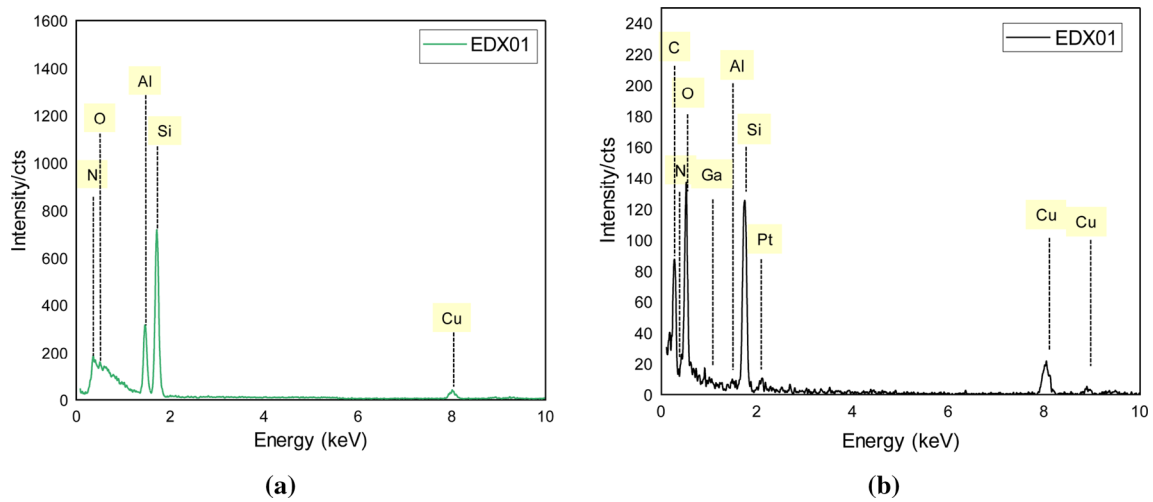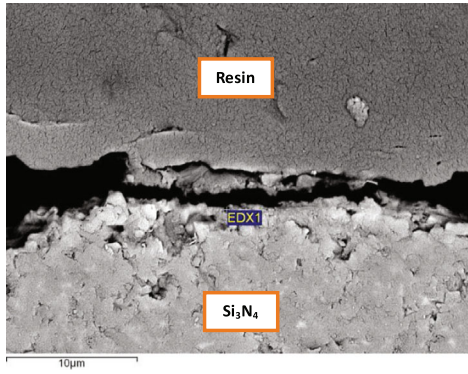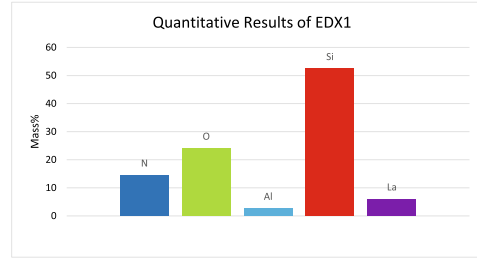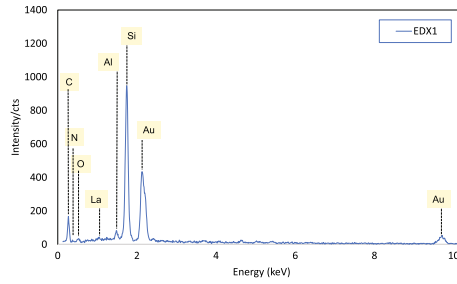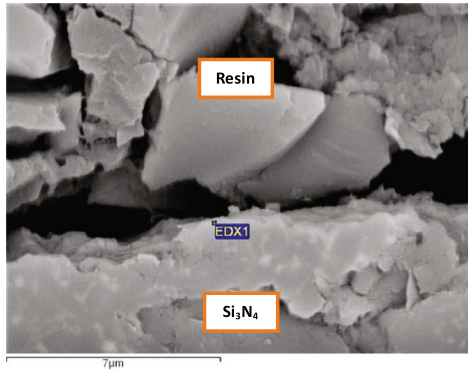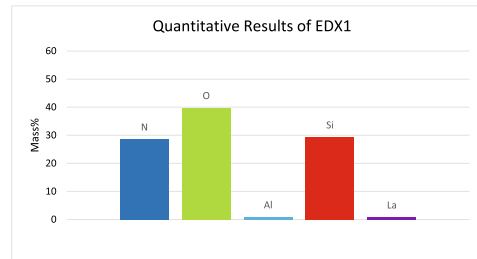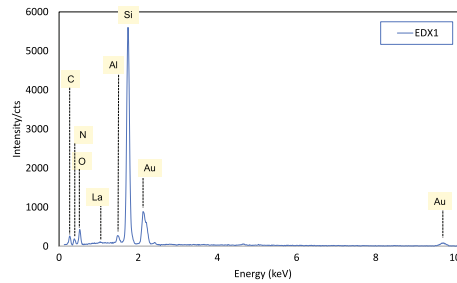

Fig. 19—EDX analysis of (*a*) spot 1 and (*b*) spot 4.

Fig. 20—SEM image of (*a*) uncoated specimen, (*b*) quantitative results of EDX analysis, (*c*) EDX spectrum and (*d*) coated specimen with removed coating, (*e*) quantitative results of EDX analysis and (*f*) EDX spectrum.
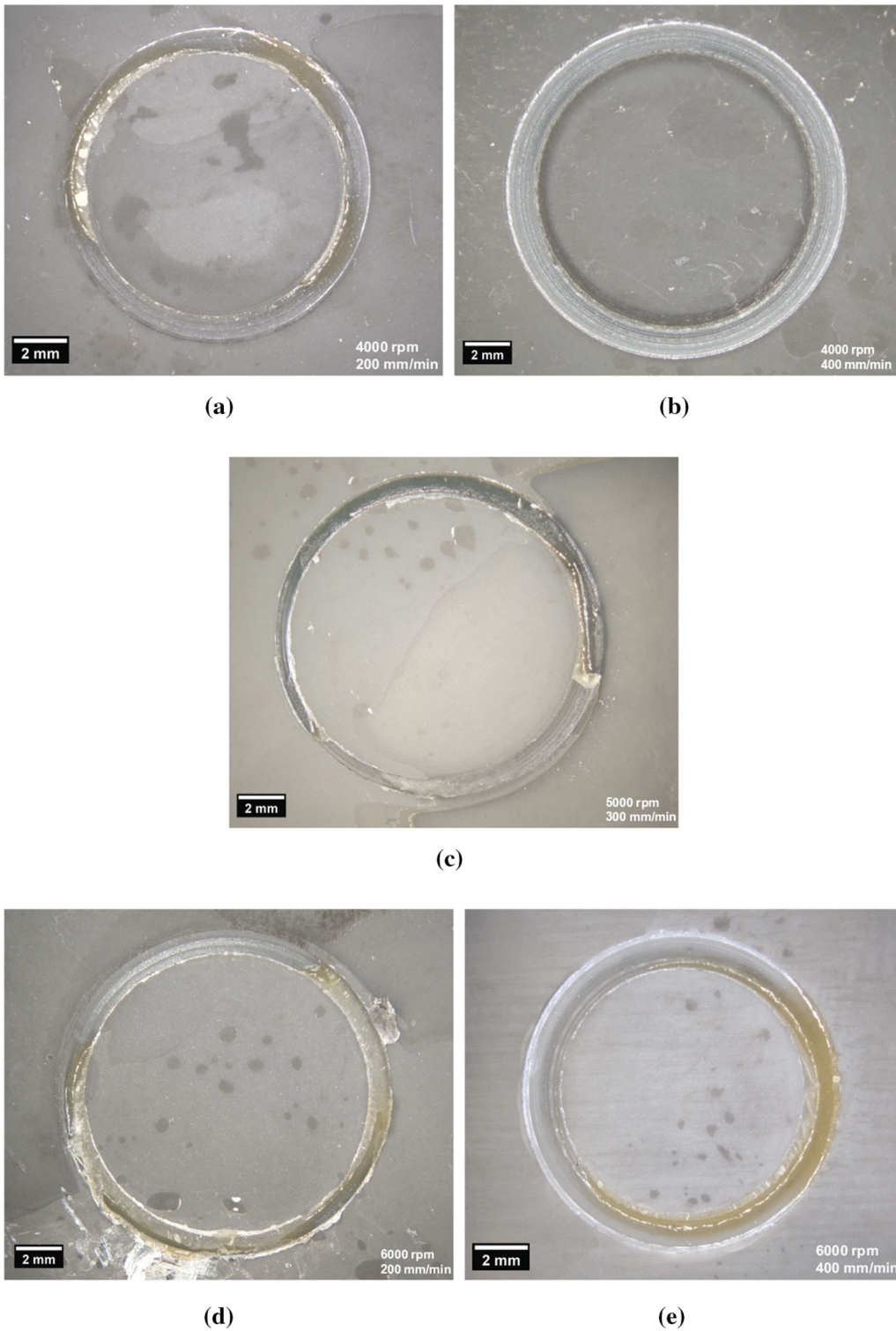
Fig. 21—Surface condition after coating pull-off for specimens with rotational speed and traverse speed of (*a*) 4000 rpm | 200 mm/min, (*b*) 4000 rpm | 400 mm/min, (*c*) 5000 rpm | 300 mm/min, (*d*) 6000 rpm | 200 mm/min and (*e*) 6000 rpm | 400 mm/min.

Si_3N_4 forming AlN and Si even at low temperatures and low annealing periods (*i.e.*, 550 ° C for 100 minutes). Also Si_3N_4 grows native oxides which are terminated by Si-OH groups on the surface when exposed to water.[54]

This hydrated substrate surface can serve as an oxide source for further reactions and formation of SiO_2 at the interface. Additionally, SiO_2 is used as an sintering additive and also segregates at the Si_3N_4 grain

Mass% of Elements

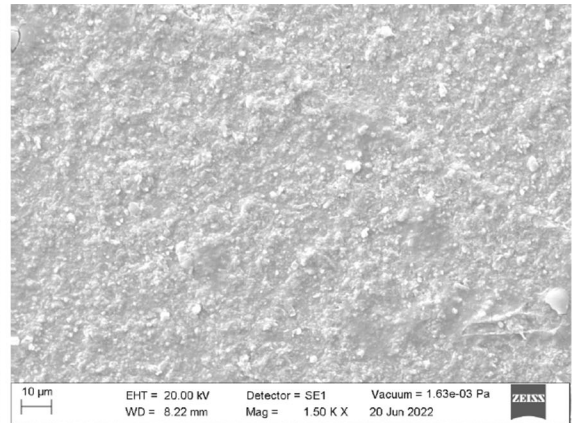| Spectrum	N	O	Mg	Al	Si
1	36.38	19.82		12.37	31.43
2	47.65	13.20		8.09	31.06
3		8.41	0.90	86.93	3.76
4		11.67	0.67	86.65	1.01

(b)
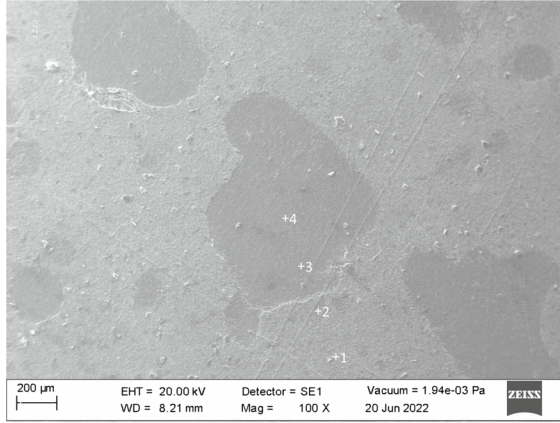
(a)
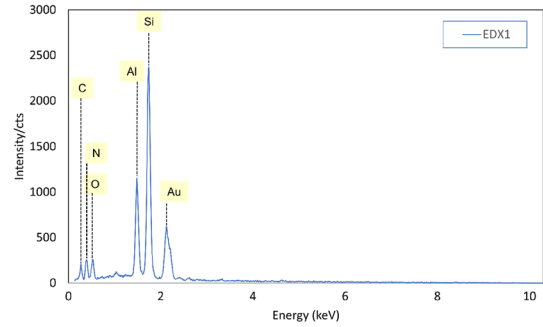
(c)

Fig. 22—SEM image of (a) pull-off dolly surface, (b) quantitative results of EDX analysis and (c) EDX spectrum at spot 1.
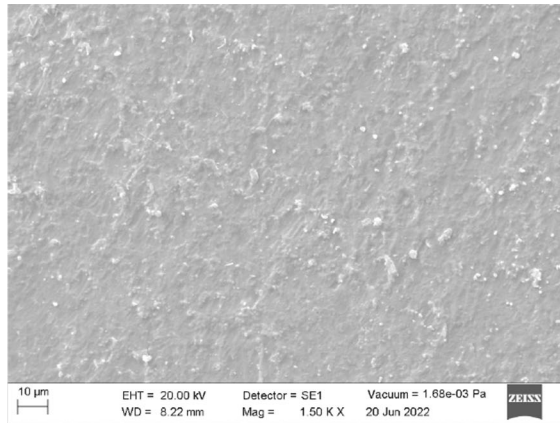
(a)

(b)

Fig. 23—SEM image of (a) spot 4 and (b) spot 1.

boundaries during the sintering process.[2] If these are exposed to the coating material additional reactions (e.g., SiAlON) can occur and form bonds at the interface.

Despite the fact that in this study no heat treatment has been carried out and the samples were only exposed to higher temperatures for a short period of time (i.e., 10 seconds), forming of new compounds at the interface has been observed. This could be due to the applied axial force and partly oxide-free coating material (Al)

coming in contact with the Si_3N_4 surface inducing a reduction reaction forming SiAlON.

Figure 24 shows a schematic diagram of the friction surfacing process, to illustrate the formation of the interfacial phases and oxides. The core material in the coating rod is not exposed to oxygen; material flow and axial force during the process brings this material in contact with the substrate surface leading to reduction of the ceramic substrate and forming of compounds even at low temperatures.
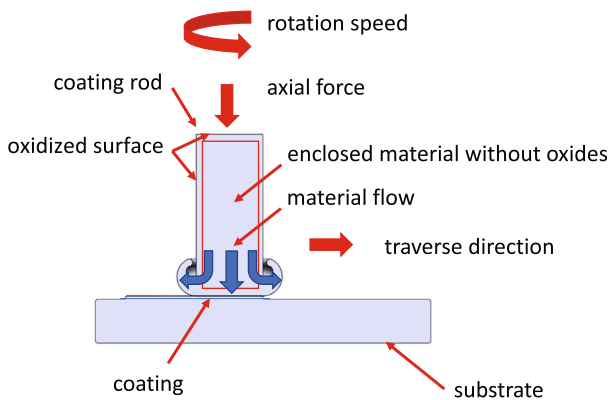
Fig. 24—Schematic diagram of the friction surfacing process explaining the formation of interfacial phases and surface oxides.

Additional experiments have been conducted by heating aluminum specimens upto 650 ° C and pushing Si_3N_4 substrates onto the surface, trying to join the parts. Due to the surface oxides of the aluminum part no reaction or bonding could be achieved. This also underlines the assumption that oxide free coating material coming in contact with the ceramic substrate is key to achieving a bond between these dissimilar materials.

For further examination of the interface composition X-ray diffraction analysis (XRD) was considered but deemed to be unsuitable because the sub-micrometer reaction zone can not be isolated properly to irradiate sufficient volume for the analysis.

IV. CONCLUSION

In this study the potential of a new low-cost, reliable and robust coating technique for ceramics based on the technique of friction surfacing has been identified. Bonding strengths and related mechanisms have been analyzed and relationships with the coating parameters have been established. Interface reactions and bonding mechanisms have been identified.

Results can be summarized as follows:

- Experiments conducted on the material combination Si_3N_4 and AlMgSi0.5 as a coating reveal that an appropriate thermal shock resistance is crucial for this type of coating process. Using Si_3N_4 no cracks have been found in the substrate.
- Additional thermal shock tests revealed crack formation at a quenching temperature of 770 K and 1000 K which was attributed to volume and surface defects as well as grain boundary weakening due to the induced thermal stress.
- *R*-squared values of 84.65 pct for the coating thickness and 80.20 pct for the bonding strength have been achieved. This indicates that the coating

process is stable across the range of input parameters used.

- Depending on the parameters used, coating thicknesses up to 2.03 mm and bonding strengths up to 42.5 MPa were achieved.
- STEM, EDX and HRTEM analysis revealed formation of a glassy phase at the interface consisting of predominantly amorphous SiAlON.
- No interface reaction was identified for low rotational speeds and high traverse speeds. Whereas by increasing the rotational speed and lowering the traverse speed an increase in interface reaction and bonded area was observed.
- Partially oxide-free coating material (Al) is exposed to the substrate surface during the coating process leading to reduction of the ceramic substrate and forming of compounds even at low temperatures.

In summary, friction surfacing of ceramics is a one step process, provides similar strength to thin-film metallizations (*e.g.*, PVD)[16] and does not require any atmospheric control or a furnace. It is also suited for low quantity production and deposition rates exceed those of physical vapor deposition by a 1000x magnitude. The applied coating can be used as is (*e.g.*, heatsink) or as a bonding agent for further process steps such as recasting, welding or brazing.

AUTHOR CONTRIBUTIONS

Not applicable.

DATA AVAILABILITY

The raw/processed data required to reproduce these findings cannot be shared at this time as the data also forms part of an ongoing study.

CODE AVAILABILITY

Not applicable.

CONFLICT OF INTEREST

ETHICAL APPROVAL

Not applicable.

INFORMED CONSENT

Not applicable.

CONSENT FOR PUBLICATION

Not applicable.

FUNDING

OPEN ACCESS

REFERENCES

1. R.B. Heimann: *Classic and Advanced Ceramics: From fundamentals to applications*, Wiley-VCH Verlag GmbH & Co. KGaA, Weinheim, Germany, 2010.
2. C.B. Carter, and M.G. Norton: *Ceramic Materials: Science and Engineering*, Second edition, Springer, New York, 2013.
3. Grand View Research, eds: Ceramics Market Size, Share & Trends Analysis Report By Product (Traditional, Advanced), By Application (Sanitary Ware, Abrasives, Tiles), By End-Use; By Region, And Segment Forecasts, 2019 - 2025. Grand View Research, 2019.
4. Versailles Project on Advanced Materials and Standards: *(VAMAS): UK, USA, CEC, Canada, Germany, France, Italy, Japan: technical report*, Wirtschaftsverl. NW Verl. für Neue Wiss, Bremerhaven, 1992.
5. M. Pfeifer: *Materials Enabled Designs: The Materials Engineering Perspective to Product Design and Manufacturing*, Butterworth-Heinemann, Amsterdam and Boston, 2009.
6. H.B. Atil, M. Leonhardt, R.J. Grant, and S. Barrans: *Proc. Inst. Mech. Eng. Part L*, 2021, vol. 235(2), pp. 366–84. https://doi.org/10.1177/1464420720965614.
7. M.B. Uday, M.N. Ahmad-Fauzi, A.M. Noor, and S. Rajoo: in *Joining technologies*, M. Ishak, ed., InTech, Rijeka, 2016.
8. H. Pulfrich: Verfahren zum vakuumdichten Verbinden von metallischen und keramischen Teilen: Patent DE000000659427A. https://depatisnet.dpma.de/DepatisNet/depatisnet?action=pdf &docid=DE000000659427A.
9. Y. Imanaka: *Multilayered Low Temperature Cofired Ceramics (LTCC) Technology*, Springer Science+Business Media Inc, Boston, MA, 2005. http://site.ebrary.com/lib/alltitles/docDetail.action?docID=10133705.
10. J.T. Klomp: in *Surfaces and Interfaces of Ceramic Materials*, L.C. Dufour, C. Monty, G. Petot-Ervas, eds., Springer, Dordrecht, 1989, pp.375–92.
11. M. Wenzel, R. Schmidt, U. Partsch, and M. Eberstein: in *Additional Conferences (Device Packaging, HiTEC, HiTEN, & CICMT). 2013*, 2013, pp. 000144–48. https://doi.org/10.4071/CICMT-WP22.
12. D.M. Mattox, and A. Short: *hort, History: Adhesion, Interface Formation, and Stress in PVD Coatings. vol. Spring, of Bulletin*, Society of Vacuum Coaters, Albuquerque, 2016.
13. A. Zalar, B.M.M. Baretzky, S. Hofmann, M. Rühle, and P. Panjan: *Thin Solid Films*, 1999, vol. 352(1–2), pp. 151–55. https://doi.org/10.1016/S0040-6090(99)00352-1.
14. C. Xin, W. Liu, N. Li, J. Yan, and S. Shi: *Ceram. Int.*, 2016, vol. 42(8), pp. 9599–9604. https://doi.org/10.1016/j.ceramint.2016.03.044.
15. R. Brener, F. Edelman, and E.Y. Gutmanas: *Appl. Phys. Lett.*, 1989, vol. 54(10), pp. 901–03. https://doi.org/10.1063/1.101418.
16. C.A. Walker, and V.C. Hodges: *Weld. J. (Miami, Fla).*, 2008, vol. 87, pp. 43–50.
17. W. Weißbach: Werkstoffkunde: Strukturen, Eigenschaften, Prüfung. 17th ed. Springer eBook Collection Computer Science & Engineering. Wiesbaden: Vieweg+Teubner; 2010. https://link-springer-com.hske.idm.oclc.org/content/pdf/10.1007%2F978-3-8348-9343-7.pdf.
18. R. Telle: *Keramik*, 7th edn. Springer, Berlin/Heidelberg, 2007.
19. BSI British Standards: Advanced technical ceramics—Methods of testing monolithic ceramics—Thermomechanical properties: BS EN 820-3, 2004.
20. D.P.H. Hasselman: *Ceramurg. Int.*, 1978, vol. 4(4), pp. 147–50. https://doi.org/10.1016/0390-5519(78)90028-5.
21. 3M Technical Ceramics: 3M Boron Carbide: Typical Material Properties. https://multimedia.3m.com/mws/media/1004125O/3m-boron-carbide.pdf.
22. Kyocera Corporation: Mechanical & Industrial Ceramics. https://global.kyocera.com/prdct/fc/product/pdf/mechanical.pdf.
23. A. Kılıçarslan, F. Toptan, I. Kerti, and S. Piskin: *Mater. Lett.*, 2014, vol. 128, pp. 224–26. https://doi.org/10.1016/j.matlet.2014.04.138.
24. J.P. Viricelle, P. Goursat, and D. Bahloul-Hourlier: *J. Therm. Anal. Calorim.*, 2000, vol. 63(2), pp. 507–515. https://doi.org/10.1023/A:1010133703284.
25. C. Varadachari, R. Bhowmick, and K. Ghosh: *ISRN Thermodyn.*, 2012, vol. 2012, pp. 1–8. https://doi.org/10.5402/2012/108781.
26. C.B. Carter, and M.G. Norton: *Ceramic Materials: Science and Engineering*, Springer Science+Business Media, LLC, New York, 2007.

27. J. Pelleg: *Mechanical Properties of Ceramics. Solid Mechanics and Its Applications*, vol. 213, Springer, Cham, 2014.
28. W. Martienssen, G. Effenberg, S. Ilyenko, G. Effenberg, H. Landolt, R. Börnstein, et al., eds.: *Numerical Data and Functional Relationships in Science and Technology: New Series. Landolt-Börnstein - Group IV Physical Chemistry*, vol. 11, Springer, Berlin, 2005.
29. S. Qu, A. Feng, L. Geng, J. Shen, and D. Chen: *Metals*, 2020, vol. 10(3), p. 420. https://doi.org/10.3390/met10030420.
30. X.M. Liu, Z.D. Zou, Y.H. ZHANG, S.Y. Qu, and X.H. Wang: *Surf. Coat. Technol.*, 2008, 202(9), pp. 1889–94. https://doi.org/10.1016/j.surfcoat.2007.08.024.
31. 3M Technical Ceramics: 3M Sintered Silicon Nitride TM: Technical Data Sheet. https://multimedia.3m.com/mws/media/1826516O/3m-advanced-materials-tds-sintered-silicon-nitride-d-cer-tds-d.pdf.
32. MR Chemie GmbH: Penetrant testing DIN EN ISO 3452-1. https://www.mr-chemie.de/wp-content/uploads/mr-produktinformationen/v_pt_process_description_en.pdf.
33. J. Antony: *Design of Experiments for Engineers and Scientists*, 2nd ed. Elsevier insights. Amsterdam, 2014. http://gbv.eblib.com/patron/FullRecord.aspx?p=1644387.
34. G.B. Barrett: *Math. Teacher*, 2000, vol. 93(3), pp. 230–234.
35. M.J.R. Stegmueller, P. Schindele, and R.J. Grant: *J. Mater. Process. Technol.*, 2015, vol. 216, pp. 430–39. https://doi.org/10.1016/j.jmatprotec.2014.10.013.
36. J. Gandra, R.M. Miranda, and P. Vilaça: *J. Mater. Process. Technol.*, 2012, vol. 212(8), pp. 1676–86. https://doi.org/10.1016/j.jmatprotec.2012.03.013.
37. M.N. Fauzi, M.B. Uday, H. Zuhailawati, and A.B. Ismail: *Mater. Design.*, 2010 vol. 31(2), pp. 670–76. https://doi.org/10.1016/j.matdes.2009.08.019.
38. M.B. Uday, M.N. Ahmad Fauzi, H. Zuhailawati, and A.B. Ismail: *Mater. Sci. Eng. A*, 2011, vol. 528(13–14), pp. 4753–60. https://doi.org/10.1016/j.msea.2011.02.091.
39. F. Edelman, E. Gutmanas, and R. Brener: *MRS Proc.*, 1989, vol. 153, p. 7. https://doi.org/10.1557/PROC-153-77.
40. Y. Mutoh, Y. Miyashita, T. Hansson, and M. Takahashi: in *Plastic Deformation of Ceramics*, R.C. Bradt, C.A. Brookes, and J.L. Routbort, eds., Springer, US, Boston, MA, 1995, pp.653–66.
41. W. Weibull: *J. Appl. Mech.*, 1951, vol. 18(3), pp. 293–297. https://doi.org/10.1115/1.4010337.
42. J. Rösler, H. Bäker, and M. Bäker: *Mechanisches Verhalten der Werkstoffe: Mit 34 Aufgaben mit Lösungen*, 3rd edn, Studium. Wiesbaden: Vieweg + Teubner, 2008.
43. ASTM Standard C1161-18: *Test Method for Flexural Strength of Advanced Ceramics at Ambient Temperature*. ASTM International, West Conshohocken, PA.
44. ASTM Standard C1499-19: *Test Method for Monotonic Equibiaxial Flexural Strength of Advanced Ceramics at Ambient Temperature*. ASTM International, West Conshohocken, PA.
45. DIN Deutsches Institut für Normung e V : Advanced technical ceramics – Mechanical properties of monolithic ceramics at room temperature – Part 1: Determination of flexural strength; German version EN 843-1:2006. DIN Deutsches Institut für Normung e.V.
46. T. Lube, and J. Dusza: *J. Eur. Ceram. Soc.*, 2007, vol. 27(2–3), pp. 1203–09. https://doi.org/10.1016/j.jeurceramsoc.2006.04.020.
47. R. Danzer, W. Harrer, P. Supancic, T. Lube, Z. Wang, and A. Börger: *J. Eur. Ceram. Soc.*, 2007, vol. 27(2–3), pp. 1481–85. https://doi.org/10.1016/j.jeurceramsoc.2006.05.034.
48. A.M. Freudenthal: *Fract. Adv. Treat.*, 1968, vol. II, pp. 591–619.
49. M. Staudacher, T. Lube, J. Schlacher, and P. Supancic: *Open Ceram.*, 2021, vol. 6, p. 100101. https://doi.org/10.1016/j.oceram.2021.100101.
50. V.K.I. Martin Hartmann: *Brevier Technische Keramik*, 4th edn., Fahner, Lauf, 2003.
51. R. Jain, J. Lock, and S.F. Duffy: in: *Proceedings of the ASME Turbo Expo 2009*. ASME, New York, NY, 2009. pp. 231–39.
52. M.F. Gazulla, M. Rodrigo, E. Blasco, and M. Orduña: *X-Ray Spectrom.*, 2013, vol. 42(5), pp. 394–401. https://doi.org/10.1002/xrs.2490.
53. P.J. Potts, J.F.W. Bowles S.J.B. Reed, and M.R. Cave, eds.: *Microprobe Techniques in the Earth Sciences*, Springer US, Boston, MA, 1995.
54. L.H. Liu, D.J. Michalak, T.P. Chopra, S.P. Pujari, W. Cabrera, D. Dick et al.: *J. Phys. Condens. Matter.*, 2016, vol. 28(9), p. 094014. https://doi.org/10.1088/0953-8984/28/9/094014.

Publisher's Note Springer Nature remains neutral with regard to jurisdictional claims in published maps and institutional affiliations.